Vector Field Heterogeneity for the Assessment of Locally Disorganised Cardiac Electrical Propagation Wavefronts From High-Density Multielectrodes

Lucía Pancorbo [iD], Samuel Ruipérez-Campillo [iD]*, Student Member, IEEE*, Álvaro Tormos [iD], Antonio Guill [iD], Raquel Cervigón [iD], Antonio Alberola [iD], Francisco Javier Chorro [iD], José Millet [iD]*, Member, IEEE*, and Francisco Castells [iD]

Abstract—High-density multielectrode catheters are becoming increasingly popular in cardiac electrophysiology for advanced characterisation of the cardiac tissue, due to their potential to identify impaired sites. These are often characterised by abnormal electrical conduction, which may cause locally disorganised propagation wavefronts. To quantify it, a novel heterogeneity parameter based on vector field analysis is proposed, utilising finite differences to measure direction changes between adjacent cliques. The proposed Vector Field Heterogeneity metric has been evaluated on a set of simulations with controlled levels of organisation in vector maps, and a variety of grid sizes. Furthermore, it has been tested on animal experimental models of isolated Langendorff-perfused rabbit hearts. The proposed parameter exhibited superior capturing ability of heterogeneous propagation wavefronts compared to the classical Spatial Inhomogeneity Index, and simulations proved that the metric effectively captures gradual increments in disorganisation in propagation patterns. Notably, it yielded robust and consistent outcomes for 4×4 grid sizes, underscoring its suitability for the latest generation of orientation-independent cardiac catheters.

Index Terms—Animal experimental models, cardiac signal processing, electrophysiology, high-density electrode catheters, vector field heterogeneity.

Impact Statement—The authors introduce the Vector Field Heterogeneity (VFH) metric, which provides a precise evaluation of disorganisation in electrical propagation maps within cardiac tissue, potentially improving the diagnosis and characterisation of electrophysiological conditions.

I. INTRODUCTION

HIGH-DENSITY grid catheters have been recently proposed for accurate characterisation of local properties of the cardia c electrophysiological substrate [1]. This grid arrangement of the electrodes allows the representation of the electrical field loop within a clique which, in turn, allows the reconstruction of orientation-independent electrograms (EGMs), also known as omnipolar EGMs (oEGMs). This technology, claimed to be orientation-independent, has been introduced to overcome some of the limitations of unipolar and bipolar EGMs [2], [3], [4]. It offers robust signals and can determine the direction of the propagation wavefront in real time, even in complex propagation patterns [5], [6]. Since the release of the Advisor HD Grid Mapping Catheter in 2016, this technology has been receiving significant attention for its use in electrophysiological explorations [7].

Examining the propagation of electrical signals within the heart provides valuable insights that can assist cardiologists in identifying conduction abnormalities and, consequently, potential catheter ablation sites [8]. In fact, the electrical propagation in healthy tissue can be locally assumed to be more homogeneous than in scarred tissue, or in arrhythmias, where disorganisation of the electrical propagation may happen. That being a key clinical concern, we propose a novel metric to assess the

heterogeneity of the propagation wavefront, by obtaining the direction of propagation in all cliques of the grid arrangement. We test it on a set of *ad-hoc* simulations of the wavefront propagation and on an animal-model with stimulated and non-stimulated propagation patterns, which allow us to analyse the behaviour of the metric on a physiological controlled environment.

Several metrics to quantify the complexity of cardiac propagation based on different properties of the signals have been proposed hitherto. For instance, entropy focuses on the complexity of EGM morphology [9] and has been used in several applications, such as to predict atrial fibrillation (AF) recurrence after pulmonary vein ablation [10], to detect complex fractionated atrial electrograms (CFAEs) [11] and rotors [12] or to discriminate paroxysmal vs. persistent AF [13], among others. Alternatively, coherence [14] and cross-correlation [15] were introduced to determine the similarity between pairs of signals, providing information on the synchronicity and coordination among different locations within the heart, which is an indicator of propagation organisation [16], [17]. The frequency spectrum of the signals has also been studied for this purpose. An example is the Organisation Index, which is based on the observation that wavelets sustaining an arrhythmia introduce additional frequency components to the spectrum [18]. This parameter was successful in guiding ablation in clinical studies [19].

Other metrics are directly applied to conduction velocities. In particular, the Anisotropy Ratio is based on the effect of impaired tissue on disrupting the normal anisotropy in conduction [20]. In addition to all these indicators, the most widely employed measurement of heterogeneity is the Spatial Inhomogeneity index, described by Lammers in 1990 [21]. This metric, based on conduction delays across the tissue, has been applied to high-density multielectrode recordings to evaluate arrhythmogenicity [22], [23], [24].

Most of these methods require a mapping system with a high number of points to provide robust and consistent measurements. Therefore, there is a need for a reliable parameter applicable to small grids, such as the 4×4 array of the Advisor HD Grid. To address this, we propose in this study the Vector Field Heterogeneity (VFH) metric, based on vector field analysis. Indeed, vector field operators such as divergence and curl have been already proposed for the analysis of propagation patterns [25]. However, it should be noted that these parameters do not measure the heterogeneity of propagation itself. Rather, they are used to identify specific patterns of interest within the maps, such as ectopic foci, wavefront collisions, or reentry circuits [26], [27].

In this article, we present the derivation of the novel VFH metric and its validation on omnipolar-derived vector maps obtained with HD grid electrode configurations. Maps for both stimulated and non-stimulated tissue are created from an experiment involving Langendorff-perfused rabbit hearts. Under the assumption that stimulation aligns the propagation vectors resulting in more organised maps, the performance of the VFH metric is based on its ability to differentiate between the two groups. Additionally, a simulation model is created to test the metric performance for different catheter sizes and levels of disorganisation under controlled conditions. Finally, the Spatial Inhomogeneity index is replicated to assess the VFH metric's potential as compared to a well-established and recognised metric.

II. MATERIALS

A. Simulated Data

Simulated propagation maps are generated to study the behaviour of the VFH metric for different grid sizes and heterogeneity levels under controlled conditions. Notably, the model does not create synthetic signals. Instead, vector maps are directly generated by assigning an angle, within a range of values with respect to a reference, to each clique in a randomised manner. That value represents the angle between that vector of propagation and the horizontal bipole with the east direction —the reference. The level of heterogeneity is therefore given by the possible angular range, which constrains the vector directions that can be generated by the model. For instance, a narrow range of $[-1°, 1°]$ implies a highly organised vector field, which will entail small heterogeneity in the map. Conversely, a broader range of $[-180°, 180°]$ allows any direction and thus implies the possibility of completely disorganised vector fields, associated with higher heterogeneity.

For a general grid, we have N vectors in a $p \times q$ clique arrangement, p being the number of cliques in a row and q the number of cliques in a column. Due to the random nature of the simulation and to avoid similar directions by coincidence, despite highly heterogeneous settings, the specified angle interval $[\theta_{lim}, -\theta_{lim}]$ is divided into N subintervals of equal length, N being the total number of cliques. Subsequently, a random angle is selected from the continuous uniform distribution contained within each subinterval and is assigned to a clique within the grid. The designation of each vector to a clique is also performed at random, which reduces the likelihood of adjacent vectors originating from contiguous subintervals.

With this model, propagation maps of different disorganisation levels were generated by increasing the value of $|\theta_{lim}|$ starting at $1°$ and from $5°$ to $180°$ in steps of $5°$. For each level, 100 maps are generated with a fixed random seed for the sake of replicability, to evaluate the global heterogeneity of the maps. Additionally, another set of 100,000 simulated maps is created to examine the trend of the heterogeneity metric in each of the steps.

B. Experimental Data

Recordings taken from Langendorff-perfused rabbit hearts have been selected for the analysis, comprising both non-stimulated (basal) and stimulated signals recorded at $37°C$, as previously described by Guill et al. [28]. Namely, an ad-hoc multielectrode mapping catheter was placed over the posterolateral wall of the left ventricular epicardium. The electrode grid consisted of 128 electrodes with 1 mm of interelectrode distance. EGMs were collected using the MapTech system at a sampling frequency of 1 kHz, following the established protocol. The cardiac tissue was stimulated at a point proximal to the left edge of the mapping catheter using a bipolar electrode connected to a GRASS S88 stimulator. To create the propagation maps,
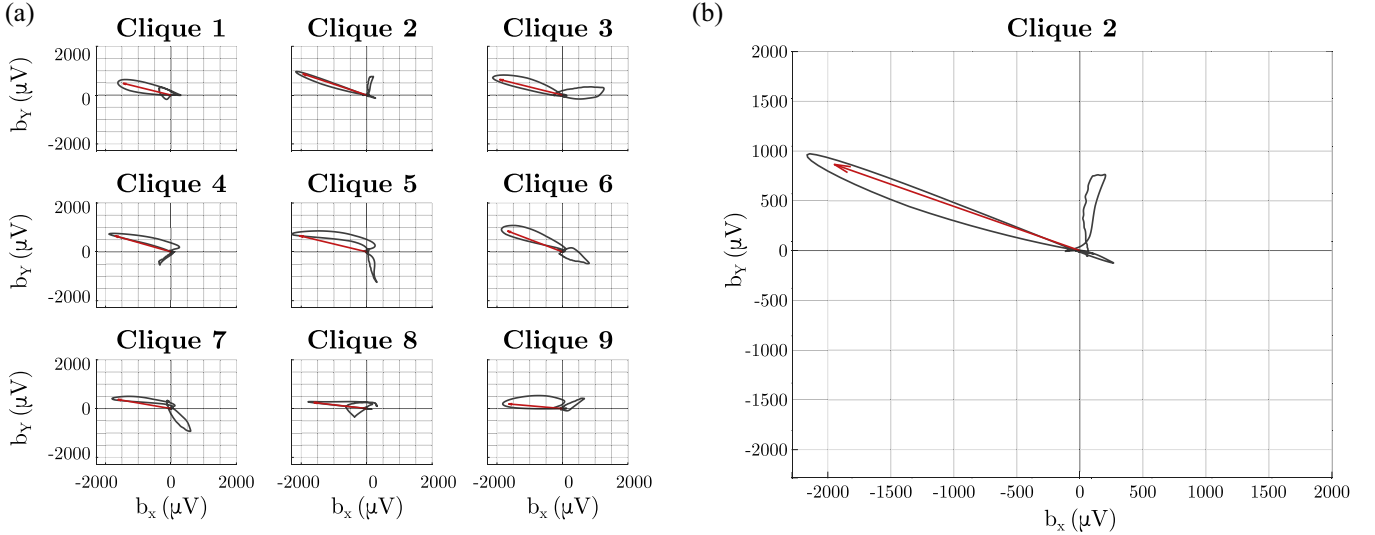
Figure 1. Representation of the bipolar loop in a recording on the epicardium of a Langendorff rabbit heart at $37\,^{\circ}$C and under stimulation of 4 Hz; (a) Loop traced by each bipole in its corresponding clique; (b) Closer look at the loop traced by the orthogonal bipoles in clique 2, with a vector indicating the estimated propagation direction for that clique.

an interval containing the activation is selected from each set of EGMs. This process results in a total of 29 propagation maps generated from basal recordings, 21 from recordings with stimulation at 4 Hz, and 18 with stimulation at 6 Hz. The protocol for the experiments was previously approved by the Ethics Committee of Universitat de Valéncia.

Initially, we considered a 4×4 subset of the electrode array from its central part, following the scheme of the Advisor HD Grid Catheter. Subsequently, we extended the grid size to investigate the metric's behaviour on various plausible electrode designs. For consistency, all grids are taken from the centre of the catheter, as the acquisition of the outermost electrodes may be less trustworthy due to possible inadequate contact with the epicardium.

III. METHODS

Non-stimulated recordings have a more heterogeneous activation pattern than stimulated recordings, given a forced alignment of the propagation vectors in the stimulated case. Therefore, we set out to establish that a metric based on vector field finite differences can effectively capture differences between groups.

A. Creation of Propagation Maps

The omnipole enables the immediate determination of the propagation direction [29]. During depolarisation, the electric field formed by the perpendicular bipoles within a clique $\mathbf{b}_x - \mathbf{b}_y$ creates the so-called bipolar loop. The loop's greatest magnitude corresponds to the direction of propagation of the wavefront [2], and is indicated by a unitary vector located at the clique's centre (see Fig. 1).

The cross-clique configuration for the omnipolar reconstruction of signals was implemented, as described in [30] and validated in an animal experimental model in [31]. From a 4×4 electrode grid and according to the definition of a clique, a 3×3

vector map is generated that displays the propagation of the wave under the catheter. The propagation angle θ is determined by the angle between each vector and the horizontal bipole $\mathbf{b}_x$. Therefore, for a specific moment in time on a matrix of $m \times n$ electrodes $G(t) \in \mathbb{R}^{m \times n}(t = c,$ for any constant $c)$, we define a matrix Φ that contains the propagation angles for each clique as:

$$\Phi \in \mathbb{R}^{p \times q} : p = m - 1, q = n - 1 \tag{1}$$

$$\theta_{i,j} : 1 \leq i \leq p, 1 \leq j \leq q \tag{2}$$

$$\Phi := \begin{bmatrix} \theta_{1,1} & \cdots & \theta_{1,q} \\ \vdots & \ddots & \vdots \\ \theta_{p,1} & \cdots & \theta_{p,q} \end{bmatrix} \tag{3}$$

Where the variables m and n denote the number of rows and columns in the matrix G, whereas p and q indicate the number of rows and columns in the matrix Φ. The indices i and j specify the position of an element within the angular matrix. Consequently, the propagation is illustrated through a map of unitary vectors that contain elements $\mathbf{u}_{i,j} = (\cos \theta_{i,j}, \sin \theta_{i,j})$.

B. Vector Field Heterogeneity

In this section we describe the proposed Vector Field Heterogeneity (VFH) metric, based on vector field analysis. Firstly, we create the 2-dimensional vector map that represents the electrical propagation, which can be split into its horizontal and vertical vector components Γ_x and Γ_y, respectively:

$$(\Gamma_x)_{i,j} = \cos \theta_{i,j}; (\Gamma_y)_{i,j} = \sin \theta_{i,j} \tag{4}$$

Where $(*)_{i,j}$ represents the element in the i-th row and j-th column of a given $p \times q$ matrix, such that $1 \leq i \leq p, 1 \leq j \leq q$.

Finite differences were used to approximate the partial derivatives of the vector field, by calculating differences between neighbouring vectors in the field. Specifically, $\Delta \Gamma_x / \Delta x$ and

$\Delta\Gamma_y/\Delta x$ were used to measure how the horizontal and vertical components vary with respect to their neighbouring points in the horizontal direction. Analogously, $\Delta\Gamma_x/\Delta y$ and $\Delta\Gamma_y/\Delta y$ were used to estimate the variation of the components with their neighbouring points in the vertical direction. Additionally, $\Delta\Gamma_x/\Delta d_1$, $\Delta\Gamma_y/\Delta d_1$ and $\Delta\Gamma_x/\Delta d_2$, $\Delta\Gamma_y/\Delta d_2$ represent the finite differences with the adjacent diagonal elements across both positive (i.e. northeast, d_1) and negative (i.e. northwest, d_2) diagonals. For the diagonal elements, a scaling factor of $\sqrt{2}$ is used to account for the spatial separation of the cliques. Forward differences of a vector field involve approximating the derivative of the field at a certain position by calculating the difference between the vector components at that point and its adjacent position at a higher index. Similarly, backward differences compute the difference between the vector components at a specific point and its neighbouring point at a lower index.

The metric derivation is based on the computation of forward and/or backward differences, depending on the point. For interior elements, that is, those which do not lie on the corner of the vector field or in the first/last row/column, the mean of the absolute forward and backward differences is computed. For edge elements, the absolute value of either the forward or backward difference is computed, depending on the edge at which the element is located. For all computations, the referred element is constrained to be within the matrix domain.

Videlicet, for a central element $(\Gamma_x)_{i,j}$:

$$\left(\frac{\Delta\Gamma_x}{\Delta x}\right)_{i,j}$$
$$= \frac{\left|(\Gamma_x)_{i,j+1} - (\Gamma_x)_{i,j}\right| + \left|(\Gamma_x)_{i,j} - (\Gamma_x)_{i,j-1}\right|}{2} \quad (5)$$

$$\left(\frac{\Delta\Gamma_x}{\Delta y}\right)_{i,j}$$
$$= \frac{\left|(\Gamma_x)_{i+1,j} - (\Gamma_x)_{i,j}\right| + \left|(\Gamma_x)_{i,j} - (\Gamma_x)_{i-1,j}\right|}{2} \quad (6)$$

$$\left(\frac{\Delta\Gamma_x}{\Delta d_1}\right)_{i,j}$$
$$= \frac{\left|(\Gamma_x)_{i-1,j+1} - (\Gamma_x)_{i,j}\right| + \left|(\Gamma_x)_{i,j} - (\Gamma_x)_{i+1,j-1}\right|}{2\sqrt{2}} \quad (7)$$

$$\left(\frac{\Delta\Gamma_x}{\Delta d_2}\right)_{i,j}$$
$$= \frac{\left|(\Gamma_x)_{i,j} - (\Gamma_x)_{i-1,j-1}\right| + \left|(\Gamma_x)_{i+1,j+1} - (\Gamma_x)_{i,j}\right|}{2\sqrt{2}} \quad (8)$$

The calculations are analogous for the matrix Γ_y. Then, the magnitude of the variations in each direction is computed to take into account both contributions Γ_x and Γ_y. Note that the magnitude variations of the vector field are scalar fields representing how each vector varies from its horizontal, vertical, and diagonal
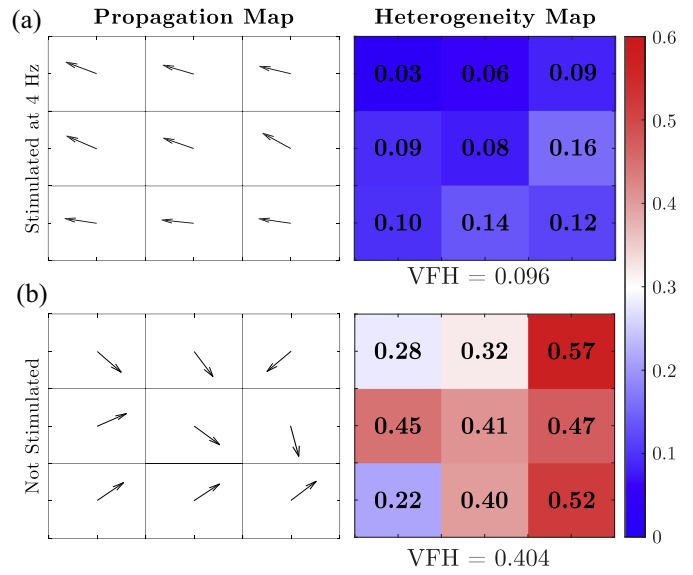

Figure 2. Illustration of heterogeneity depicting the heterogeneity scores of each clique $(\Psi)_{i,j}$ and the VFH value assigned to the map; (a) Results for a recording stimulated at 4 Hz, with the propagation vector map (left) and the heterogeneity map (right), illustrating an organised region of propagation; (b) Idem for a basal recording where the propagation map is found to be more disorganised.

neighbours respectively, that is:

$$\left(\frac{\Delta\mathbf{\Gamma}}{\Delta x}\right)_{i,j} = \sqrt{\left(\frac{\Delta\Gamma_x}{\Delta x}\right)_{i,j}^2 + \left(\frac{\Delta\Gamma_y}{\Delta x}\right)_{i,j}^2} \quad (9)$$

$$\left(\frac{\Delta\mathbf{\Gamma}}{\Delta y}\right)_{i,j} = \sqrt{\left(\frac{\Delta\Gamma_x}{\Delta y}\right)_{i,j}^2 + \left(\frac{\Delta\Gamma_y}{\Delta y}\right)_{i,j}^2} \quad (10)$$

$$\left(\frac{\Delta\mathbf{\Gamma}}{\Delta d_1}\right)_{i,j} = \sqrt{\left(\frac{\Delta\Gamma_x}{\Delta d_1}\right)_{i,j}^2 + \left(\frac{\Delta\Gamma_y}{\Delta d_1}\right)_{i,j}^2} \quad (11)$$

$$\left(\frac{\Delta\mathbf{\Gamma}}{\Delta d_2}\right)_{i,j} = \sqrt{\left(\frac{\Delta\Gamma_x}{\Delta d_2}\right)_{i,j}^2 + \left(\frac{\Delta\Gamma_y}{\Delta d_2}\right)_{i,j}^2} \quad (12)$$

The heterogeneity score matrix Ψ is computed by adding the four magnitude matrices. To normalise the values, each resulting element is divided by its corresponding upper bound.

$$(\Psi)_{i,j} = \frac{\left(\frac{\Delta\mathbf{\Gamma}}{\Delta x}\right)_{i,j} + \left(\frac{\Delta\mathbf{\Gamma}}{\Delta y}\right)_{i,j} + \left(\frac{\Delta\mathbf{\Gamma}}{\Delta d_1}\right)_{i,j} + \left(\frac{\Delta\mathbf{\Gamma}}{\Delta d_2}\right)_{i,j}}{(\xi)_{i,j}}$$
$$0 \leq (\Psi)_{i,j} \leq 1 \quad (13)$$

The normalisation constant ξ of size $p \times q$ contains the upper bounds of each element, which are the same for all positions except for the vertices:

$$(\xi)_{i,j} = \begin{cases} 4 + \sqrt{2} & i \in \{1, p\} \text{ and } j \in \{1, q\} \\ 4 + 2\sqrt{2} & \text{elsewhere} \end{cases} \quad (14)$$

$(\Psi)_{i,j}$ is assigned to the corresponding propagation map element, indicating how dissimilar that vector is from the surrounding vectors (see Fig. 2). Finally, all elements are averaged to
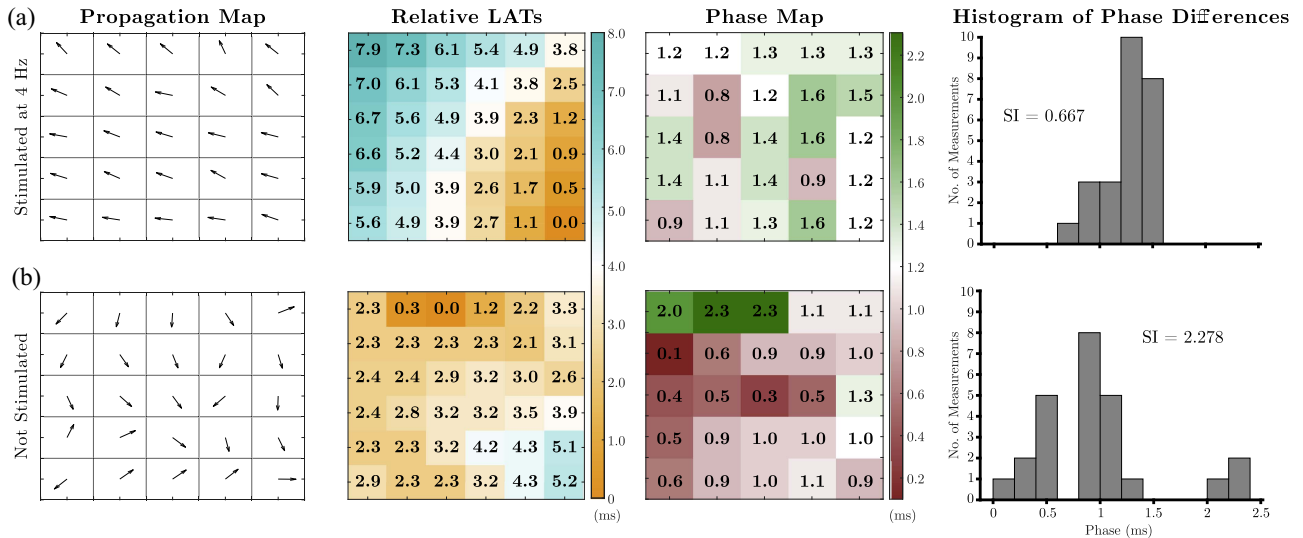
Figure 3. Calculation of the Spatial Inhomogeneity (SI) index, proposed by Lammers et al., for a 6×6 grid of recordings depicted in Fig. 2; (a) Results for a recording stimulated at 4 Hz, with the propagation vector map (first column), Local Activation Time relative to the earliest LAT of the map, for representation purposes (second column), the corresponding phase map (third column), and the phase differences histogram (last column); (b) Idem for a basal recording.

obtain the heterogeneity value VFH, which is assigned to the whole local map:

$$\text{VFH} = \frac{\sum_{i=1}^{p} \sum_{j=1}^{q} (\Psi)_{i,j}}{p \cdot q} : 0 \leq \text{VFH} < 1 \qquad (15)$$

Note that VFH is not meant to reach 1 because that would imply that all the elements $(\Psi)_{i,j}$ are equal to 1. According to the definition, an element of the map has a value of 1 when all its adjacent vectors point in the opposite direction, which in turn prevents them from having the maximum score of 1 when analysing other adjacent pairs.

C. Metric Comparison With the Widely Accepted Spatial Inhomogeneity Index

The proposed VFH metric is compared to the widely adopted Spatial Inhomogeneity (SI) index [21], commonly used in the literature. This index was introduced more than three decades ago to quantify cardiac conduction disorders using activation maps derived from high-density recordings. To replicate the methodology, local activation times were mapped to each electrode position by timing the $-dV/dT_{\max}$ of the unipolar EGMs [32]. A phase difference, also known as activation time-delay, is defined as the temporal variation between activation times and is measured in *ms* [33]. To create a phase map, phase differences were calculated between each pair of electrodes forming a clique and the largest value was assigned to that position. The resulting map represents the spatial distribution of conduction inconsistencies. Finally, local phase differences were represented in a histogram. The total range of differences, computed as $P_{95} - P_5$, is the absolute inhomogeneity. This parameter might increase due to a global decrease in conduction velocities, so the SI index $(P_{95} - P_5)/P_{50}$ is used to represent inhomogeneities in conduction independent of the velocities.

To assess this metric's performance and compare it to the proposed one, inhomogeneity indexes were computed for recordings in the experimental data set (see Fig. 3). The ability of the index to distinguish between basal and stimulated groups is studied. Observe that the mapping catheter possesses a unit interelectrode distance with phase differences calculated solely between adjacent electrodes, excluding the diagonal elements. Consequently, their values are inherently normalised to 1 mm.

D. Statistical Analysis

The ability of the proposed metric to distinguish between populations based on stimulation type was evaluated to reveal its potential as a heterogeneity metric. The resulting VFH values are tested for statistical differences across the three groups: basal, stimulation at 4 Hz, and stimulation at 6 Hz. The same analysis is performed on the SI index to provide an objective comparison between the two metrics.

The Wilcoxon rank-sum test (5% significance level) was applied to perform multiple comparisons on the resulting heterogeneity distributions (see Figs. 5 and 7). The Wilcoxon rank-sum test is a non-parametric alternative to the Analysis of Variance (ANOVA) test. Typically, one-way ANOVA would be employed to assess differences in the means of heterogeneity values across the groups, with the type of stimulation being the independent variable. However, due to the limited number of samples in the experimental dataset, the assumption of normality required by ANOVA is not satisfied. This was verified through the Shapiro-Wilk test and examination of the QQ plots (see Appendix A). A similar analysis was conducted to study the effect of the catheter size on the metric's performance. In this case, the independent variable was the size, and multiple comparisons between consecutive grid sizes were performed. In order to account for multiple testing, the Bonferroni correction was applied to adapt
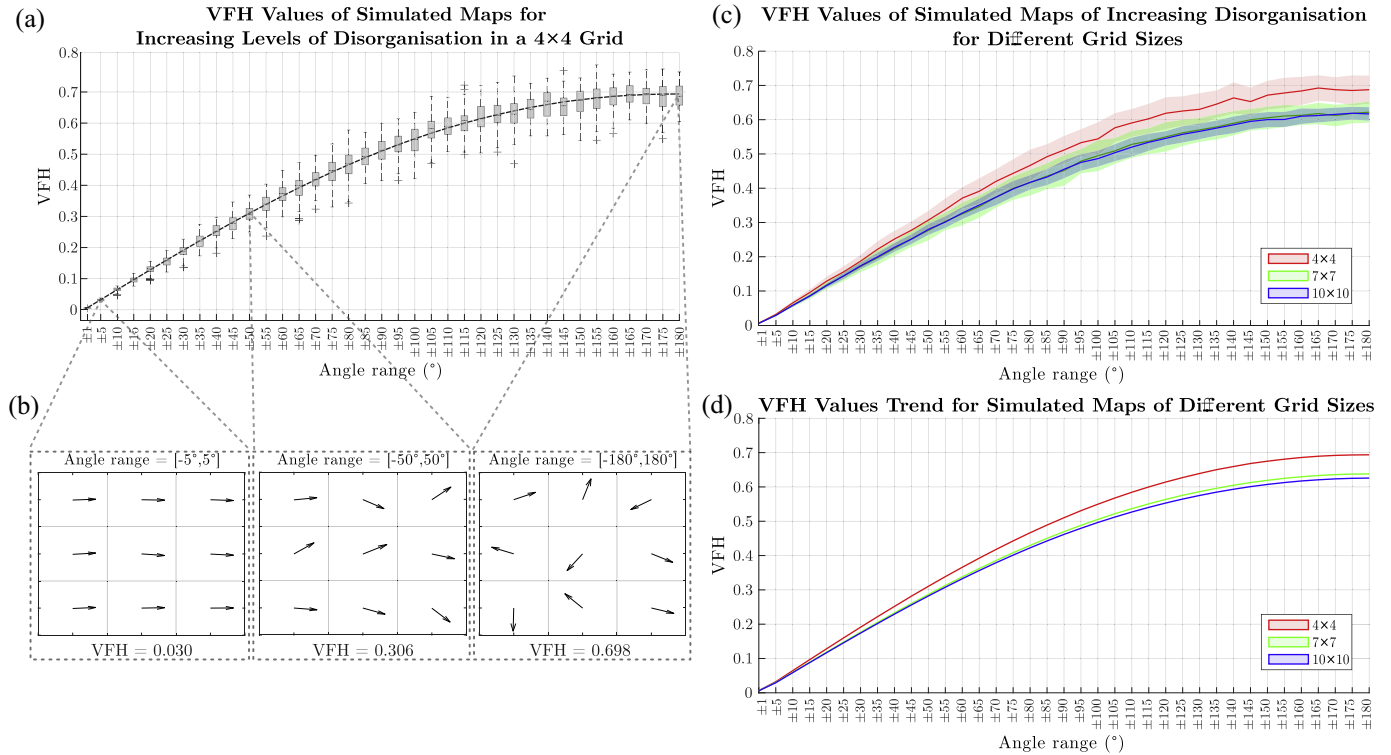
(a)

(b)

(c)

(d)

Figure 4.   (a) Box and whisker plot of the VFH values of simulated propagation maps of increasing disorganisation. For each angle range, 100 simulations were performed corresponding to a 4×4 catheter grid. The trend of the VFH metric (dashed line) is calculated by running 100,000 simulations for each interval and plotting the mean VFH value; (b) Propagation maps representative of three distinct angle ranges; (c) Comparison of the VFH values from simulated propagation maps of different catheter sizes. The shaded region corresponds to the standard deviation and the line is the mean VFH value for the 100 simulations. The decrease in standard deviation from 4×4 to 10×10 is to be highlighted; (d) Trends are calculated by taking the mean VFH value from 100,000 simulations for each angle range.

the p-values based on the number of comparisons. The values for VFH and SI are summarised in the medians and interquartile ranges (IQR) arising from the Wilcoxon test.

The Receiver Operating Characteristic (ROC) curves were generated for both metrics to compare their effectiveness in distinguishing between basal and stimulated cases. The Area Under the Curve (AUC) was provided to measure the overall performance of the classifiers. For this analysis, stimulated at 4 Hz and 6 Hz results were grouped, resulting in an imbalanced set -29 basal; 39 stimulated. For this reason, Precision-Recall (PR) curves and their respective AUCs were also examined, as they may provide more meaningful insights in the presence of class imbalance.

IV. RESULTS

A. Simulations

The VFH metric's behaviour for a 4×4 electrode grid — which leads to a 3×3 clique grid— is studied by computing the VFH value of simulated maps of increasing heterogeneity (Fig. 4(a)). It can be observed that widening the angle interval results in higher VFH values, which are representative of greater disorganisation of the vectors (see Fig. 4(b)). Running 100,000 simulations provides a close approximation of the trend of the metric (dashed line). It shows a linear behaviour until $45°$ with a slope of 0.0315, computed through linear regression. After that

point, the progression curves and smooths out until VFH reaches a value around 0.7 for a completely random set-up. Note that while 0.7 represents the average value for highly disorganised maps, it is not the maximum achievable value. The highest recorded VFH value from among the 100,000 simulations at $180°$ is 0.7933, which represents an empirical upper bound of the metric.

Simulated maps of different sizes were generated to study the impact of increasing the number of data points on the metric's behaviour (Fig. 4(c)). The VFH values obtained for different catheter sizes are displayed together, comparing the previous results with those obtained from 7×7 and 10×10 grid sizes. It can be appreciated that using larger grids leads to a decrease in the standard deviation. The three trends have similar shapes, following a linear behaviour for the first points and then reaching a plateau (Fig. 4(d)). However, some differences can be observed for the larger grids. The initial linear trend has a lower slope and they converge to a lower value of VFH = 0.62, approximately. The maximum values recorded at $180°$ are 0.7262 and 0.6911 for 7×7 and 10×10 grids, respectively.

B. Experimental Data

Fig. 5 illustrates the distribution of VFH values for different stimulation types using electrode grids of increasing size. Table I collects the median and IQR values for each case. For
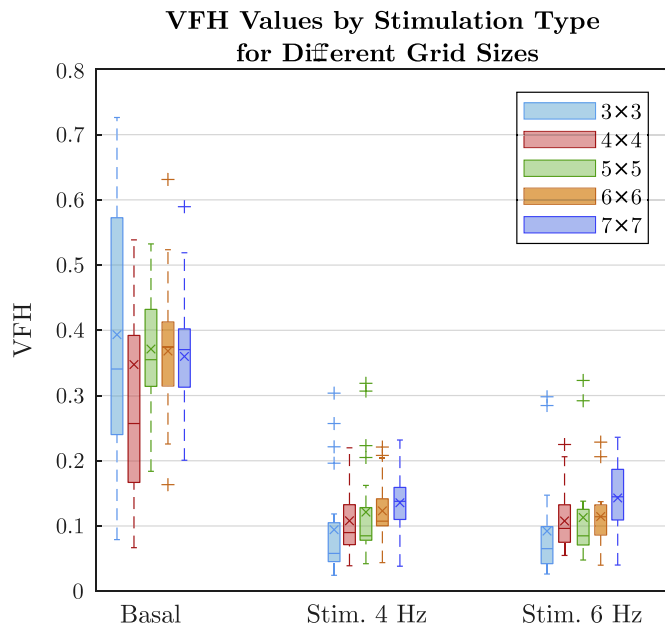
Figure 5. Box and whisker plots of the VFH values according to the type of stimulation. Results for different catheter sizes are shown.

TABLE I
VFH VALUES FOR DIFFERENT GRID SIZES ACCORDING TO THE STIMULATION TYPE

Size	Basal Median	Basal IQR	Stim. 4 Hz Median	Stim. 4 Hz IQR	Stim. 6 Hz Median	Stim. 6 Hz IQR
3×3	0.341	0.334	0.058	0.065	0.065	0.064
4×4	0.323	0.228	0.090	0.071	0.096	0.063
5×5	0.355	0.126	0.085	0.062	0.085	0.056
6×6	0.375	0.102	0.107	0.043	0.114	0.048
7×7	0.370	0.092	0.138	0.049	0.145	0.078

TABLE II
P-VALUES OF WILCOXON RANK-SUM TEST FOR COMPARING VFH VALUES ACCORDING TO STIMULATION TYPE

Catheter Size	Basal - Stim. 4 Hz	Basal - Stim. 6 Hz	Stim. 4 Hz - Stim. 6 Hz
3×3	2.8938e-07*	1.0024e-06*	0.8547
4×4	1.6878e-08*	4.7571e-08*	0.8547
5×5	1.6878e-08*	6.8712e-08*	0.7037
6×6	3.7057e-09*	1.7482e-08*	0.5447
7×7	3.7057e-09*	1.9845e-08*	0.5447

* p-values < 0.0167

a 4×4 grid, the VFH value tends to be approximately 0.35 without stimulation. Conversely, when the heart was stimulated, the value decreased to 0.11 on average. Significant differences are observed between the results of the basal group and both stimulated groups. However, there is no statistical difference between stimulations at 4 Hz and 6 Hz. This is consistent for all catheter sizes (see Table II). For a total of 3 comparisons and applying the Bonferroni correction, the null hypothesis, describing lack of difference among results, is rejected for p < 0.0167.

When expanding the analysis to include more electrodes, we observe that the mean VFH value remains constant for the basal groups, whereas there is a slight increase in the stimulated cases.

TABLE III
P-VALUES OF WILCOXON RANK-SUM TEST FOR COMPARING VFH VALUES ACCORDING TO CATHETER SIZE

Catheter Size	3×3 - 4×4	4×4 - 5×5	5×5 - 6×6	6×6 - 7×7
Basal	0.3924	0.4010	0.9010	0.5650
Stim. 4 Hz	0.0826	0.9198	0.2177	0.0826
Stim. 6 Hz	0.0847	0.6693	0.2750	0.0642

* p-values < 0.0125

TABLE IV
SI VALUES FOR DIFFERENT GRID SIZES ACCORDING TO THE STIMULATION TYPE

Size	Basal Median	Basal IQR	Stim. 4 Hz Median	Stim. 4 Hz IQR	Stim. 6 Hz Median	Stim. 6 Hz IQR
3×3	0.909	0.705	0.455	0.455	0.545	0.336
4×4	1.200	0.783	0.643	0.515	0.652	0.296
5×5	1.680	0.634	0.862	0.460	0.807	0.368
6×6	1.917	0.648	0.731	0.522	0.773	0.457
7×7	1.850	0.684	0.800	0.779	0.836	0.560

Furthermore, as the grid size is increased, the standard deviation of the VFH value decreases for the basal group, but is maintained for stimulation at 4 Hz and 6 Hz.

The statistical analysis reveals there is no significant difference in the VFH values when increasing the electrode grid in one unit (i.e. from 3×3 to 4×4). Table III shows the p-values obtained from applying the Wilcoxon Rank-Sum test on the 4 comparisons. The null hypothesis is rejected when the p-value is lower than the significance level after the Bonferroni correction (p-value < 0.0125).

An example of a propagation map acquired by an 8×8 electrode grid is shown in Fig. 6. The map shows local differences in heterogeneity which are quantified using a 4×4 grid (Fig. 6(a)). A value of VFH = 0.64 is found for the disorganised region, compared to VFH = 0.07 in the homogeneous area. This local evaluation using a smaller grid is compared to a global quantification of the whole map that results in a value of VFH = 0.23 (Fig. 6(b)).

C. Metric Comparison

Fig. 7 shows the resulting SI index values for different stimulation types and for electrode grids of increasing size. Table IV collects the median and IQR values for each case. In the case of a 4×4 catheter size, the resulting index has a mean value of 1.46 for basal recordings. When there is stimulation, this value decreases to an average of 0.87 for both frequencies. Similarly to the VFH values, the SI indexes obtained for the basal groups are statistically different to those from stimulated groups. Additionally, no significant difference exists between stimulation at 4 and 6 Hz. This relationship is maintained for different grid sizes (see Table V).

When comparing the results between different catheter sizes, there were only significant differences (p-value ≤ 0.0125) found between 3×3 - 4×4, and 4×4 - 5×5 for the basal cases, and between 3×3 - 4×4 for stimulation at 4 Hz (see Table VI).

Given the lack of statistical difference between stimulation at 4 Hz and at 6 Hz revealed by the previous analysis, both
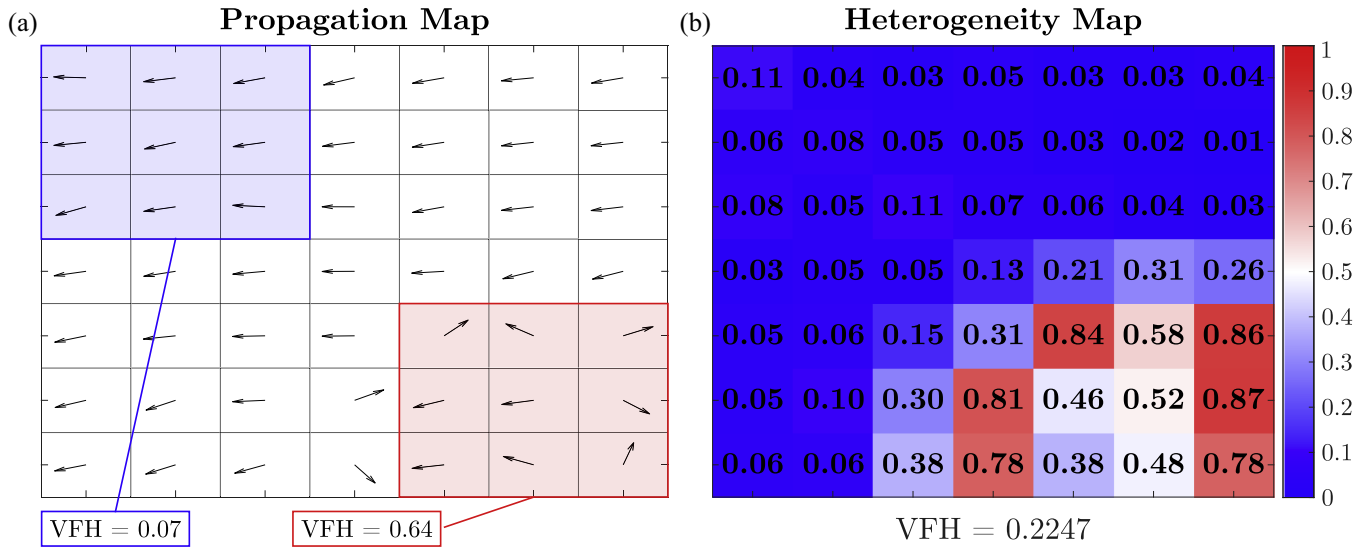
(a)

Propagation Map

VFH = 0.07

VFH = 0.64

(b)

Heterogeneity Map

VFH = 0.2247

Figure 6. Example of heterogeneity analysis for an 8×8 catheter grid; (a) Vector map representing propagation under the catheter. The VFH values that a 4×4 grid would obtain are displayed; (b) Heterogeneity Map displaying the heterogeneity values assigned to each vector $(\Psi)_{i,j}$ and the global VFH value of the whole map.
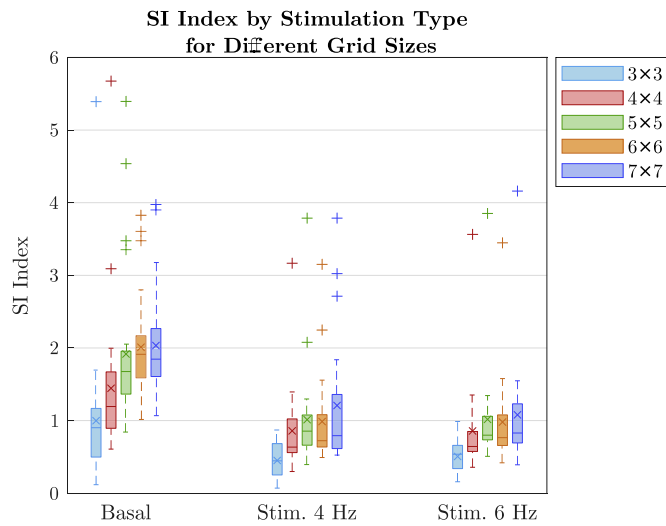
SI Index by Stimulation Type for Different Grid Sizes

Figure 7. Box and whisker plots of the SI index values according to the type of stimulation. Results for different catheter sizes are shown.

groups were merged and the effectiveness of the metrics as binary classifiers basal/stimulated was compared. As depicted in Fig. 8(a), the ROC curve for the VFH metric is further away from the diagonal than the ROC curve obtained for the SI index. This results in a higher AUC value for the proposed metric for all catheter sizes (see Table VII, upper panel).

Furthermore, a PR curve is computed to address possible inaccuracies from the imbalanced data set. The PR curves show similar behaviour to the ROC analysis (see Fig. 8(b)), with higher AUC values for the proposed metric despite the catheter size. These values are displayed in Table VII (bottom pannel) and the curves for all sizes are shown in Appendix A.

TABLE V

P-VALUES OF WILCOXON RANK-SUM TEST FOR COMPARING SI INDEXES ACCORDING TO STIMULATION TYPE

Catheter Size	Basal - Stim. 4 Hz	Basal - Stim. 6 Hz	Stim. 4 Hz - Stim. 6 Hz
3×3	9.5733e-04*	0.0078*	0.4302
4×4	2.0249e-04*	5.3850e-05*	0.8546
5×5	7.4016e-06*	3.6776e-06*	0.7247
6×6	2.8853e-06*	1.5517e-06*	0.6829
7×7	5.5782e-05*	1.7295e-06*	0.9663

* p-values < 0.0167

TABLE VI

P-VALUES OF WILCOXON RANK-SUM TEST FOR COMPARING SI INDEXES ACCORDING TO CATHETER SIZE

Catheter Size	3×3 - 4×4	4×4 - 5×5	5×5 - 6×6	6×6 - 7×7
Basal	0.0025*	0.0025*	0.0885	0.9690
Stim. 4 Hz	0.0028*	0.1703	0.6966	0.6060
Stim. 6 Hz	0.0176	0.0598	0.7637	0.5797

* p-values < 0.0125

(a)

ROC Curves

(b)

PR Curves

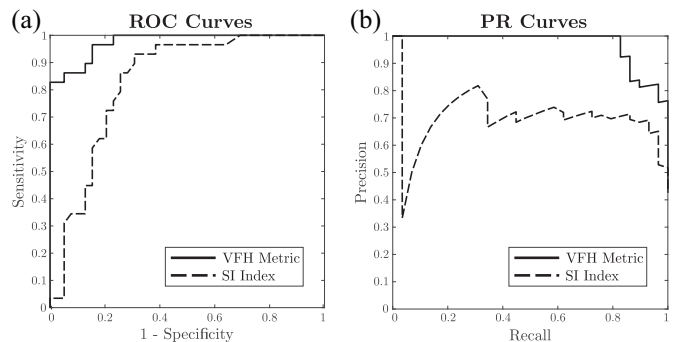**Figure 8.** (a) ROC curves comparison between the VFH metric proposed in this study (solid line) and the SI index (dashed line) for the case of a 4×4 electrode grid; (b) Same comparison for the PR curves.

TABLE VII
AUC VALUES FOR THE ROC AND PR CURVES

ROC Curves		
Catheter Size	VFH Metric	SI Index
3×3	0.9293	0.7569
4×4	0.9752	0.8311
5×5	0.9726	0.8895
6×6	0.9938	0.9054
7×7	0.9929	0.8753
PR Curves		
Catheter Size	VFH Metric	SI Index
3×3	0.9165	0.7903
4×4	0.9709	0.7014
5×5	0.9640	0.7764
6×6	0.9928	0.8088
7×7	0.9914	0.7024

V. DISCUSSION

In this study, we propose the VFH, a heterogeneity metric based on vector field analysis to characterise the local electrophysiological substrate. This parameter is computed from omnipolar-derived vector maps obtained with HD grid electrodes. Although it has been designed to provide robust results in small-size arrays, it can be easily adapted to catheters of any size and even to other electrode arrangements through simple parameter adjustments.

The properties of the VFH metric were first explored on simulated maps with progressively higher levels of disorganisation. This allows for objective assessment under controlled conditions. In this case, the success of the VFH parameter is proven by its ability to reflect the increasing disorganisation of simulated maps. The curve evolution as well as the standard deviation ranges allow us to obtain a deep understanding of the metric. Furthermore, the asymptotic behaviour at high complexity lets us assign an empirical upper bound for this parameter, which is rather unpractical to derive as a closed-form solution. In contrast, the SI index is not upper-bounded, which may lead to outliers that could bias statistical results, as can be appreciated in Fig. 7. Moreover, the performance of the VFH metric with different grid sizes was explored. Interestingly, the VFH maintained its robustness when applied to small maps as compared to larger grid sizes, as can be appreciated in Fig. 4. Nevertheless, there is some decrease in the VFH values when increasing the grid size to 7×7 due to an averaging effect with a higher number of vectors. Accordingly, comparison of VFH values obtained with different grid sizes should be avoided.

The validation of the metric on the experimental data depends on its ability to distinguish between basal (not organised) and stimulated (organised) maps. Both the VFH metric and the SI index provide significant differences between the two groups. However, this distinction is less noticeable in the SI, as can be inferred from the p-values (Tables II and V) and a higher overlapping of the box and whiskers plots between basal and stimulated groups. The ROC analysis confirms the superiority of VFH, obtaining greater AUC values than the SI index for all sizes. An equivalent conclusion is obtained from the PR curves, which support the previous results despite class imbalance. Moreover,

the SI index has larger standard deviations (and outliers, as aforementioned) than the VFH, which implies a less accurate and more inconsistent characterisation of propagation. Moreover, SI values were also dependent on catheter size (Tables III and VI).

The caveats of the SI index could be understood by the fact that it is derived from LAT maps [21]. A disadvantage of this methodology is that in the case of complex EGMs, LATs might be difficult to define [33], hence introducing high variability with different LAT detection methods. It might be questioned whether the reported differences between the VFH and the SI index are primarily driven by inconsistencies in LAT determination. To investigate this hypothesis, VFH values were computed using LAT-derived vector maps. As observed in Appendix B, these differences persist, even upon negating the impact of LAT errors. This suggests that the enhanced performance of the VFH metric relative to the established SI index is intrinsic to its properties, thus solidifying its validation.

Other studies have been primarily focused on measuring the complexity of EGM morphology by means of entropy measurements [34]. However, further research is needed to better understand the origins of CFAEs [35]. Alternative metrics, like Coherence or Cross-Correlation [15], [36], compare simultaneous recordings from separate points of the cavity. Nevertheless, this requires the use of larger grids, which may be a limiting factor. On the other hand, conduction velocity metrics, such as the Anisotropy Ratio [20], require mapping a high amount of data points [37], [38].

This analysis of heterogeneity in propagation is of great interest in clinical settings. A main focus could be the detection of impaired areas such as fibrotic tissue, given the fact that fibrosis disrupts the uniform propagation of the signals [39], thus causing an arrhythmogenic substrate. Its potential to identify arrhythmia drivers and therefore offer assistance in planning ablation procedures, is also a major clinical problem where this method could be useful.

Furthermore, major works have been recently proposed to understand and characterise the organisation of wavefront propagation based on intracardiac recordings. In particular, the study by Ganesan et al. [40] defines a novel metric coined as REACT to evaluate the size of the areas containing synchronised EGMs, shown to be predictive of ablation outcomes. Shortly afterwards, a similar analysis proposes Repetitive Atrial Activation Patterns (RAAPs), found to be associated with arrhythmia drivers [41]. This increasing interest in developing metrics to quantify cardiac organisation highlights the relevance of prior tissue characterisation for better planning and guidance of cardiac interventions.

A. Limitations and Future Work

The retrospective nature of the experiment, together with the quality selection of the recordings, has resulted in a restricted sample size for the experimental data set. Additionally, epicardial signals may fail to capture the electrophysiological reality of intracardiac propagation. Nevertheless, the statistical analysis produced encouraging results which will likely improve by expanding the data set, preferably using intracardiac signals
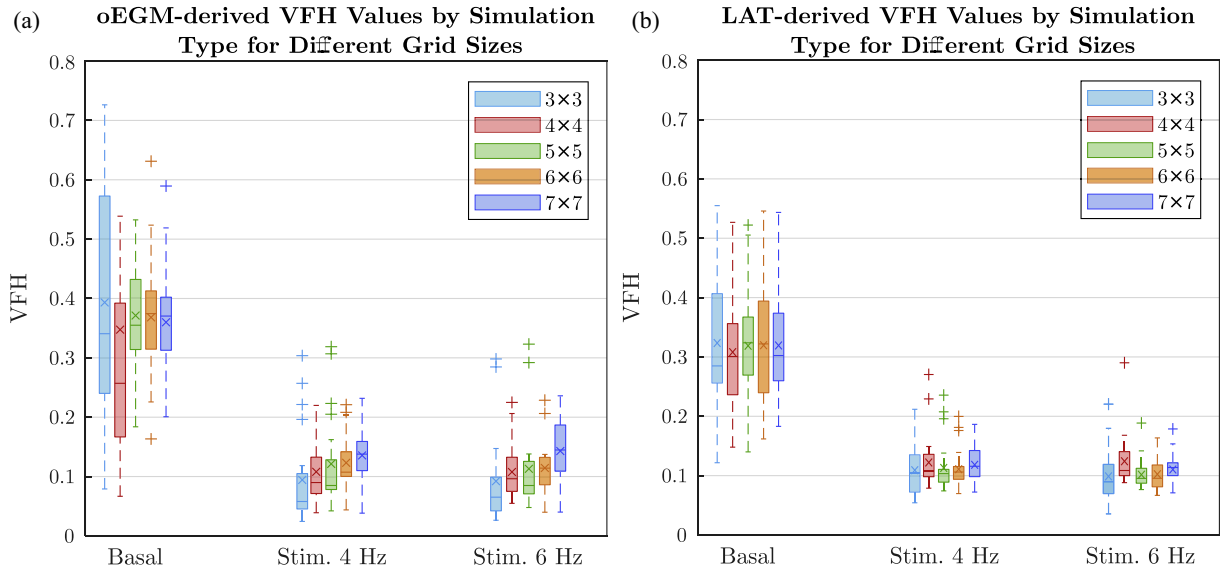
Figure 9. Box and whisker plots of the VFH values according to the type of stimulation. Results for different catheter sizes are shown; (a) Application of VFH metric to omnipolar-derived vector maps; (b) Application of the metric to LAT-derived vector maps.

from larger animal species that better resemble the physiological characteristics of the human heart.

With respect to the simulation model, its design focuses on generating propagation maps specifically for the VFH metric, thereby limiting the ability to test alternative metrics that are not defined on vector maps. A more complex model, capable of producing propagation patterns based on activation times or synthetic EGMs, would enable the evaluation of the SI index using simulated data. By employing this alternative model, it would be possible to compare the behaviours and trends of both metrics, providing a more comprehensive analysis for validation purposes.

The success of the Vector Field Heterogeneity to quantify disorganised patterns in this specific application suggests that this metric could be valuable in other applications related to vector fields. Indeed, vector field analysis has been applied not only to the characterisation of bio-electrical field patterns but also to problems related to magnetic flux [42], wave propagation and fluid flow [43], [44], among others. Whereas the most common parameters employed in vector field analysis involve divergence and curl, which aim to find organised patterns such as whirls [25] and focal sources [45] or sinks [46], the proposed parameter could well be proposed as a complementary metric that intends to detect disorganised and chaotic behaviours. Therefore, and for the sake of generalisability, future work focusing on the development of a theoretical framework of the VFH metric would be valuable. This should include its definition in a continuous form and its subsequent discretisation in an N-dimensional space. Additionally, its properties could be thoroughly contrasted with those of the well-established parameters divergence and curl to highlight their differences as well as their similarities, concluding with suggestions and indications of typical scenarios where to exploit the potential of VFH.

Future work could take the direction of implementing a versatile tool for quantifying heterogeneity in a wider range of vector field-related problems. We could then explore the potential applications of the VFH metric, such as its ability to differentiate between fibrotic and healthy tissue on the surface or through the cavities' wall.

An additional approach would be to explore the implementation of the metric beyond grid arrays. Since there exists a wide variety of catheters, incorporating the metric to the most commonly used types would enhance its applicability and potential. Thus, it is important to define the necessary adjustments and determine if comparable results are achieved.

VI. CONCLUSION

Measuring the disorganisation of propagation vector maps presents a promising method for cardiac tissue characterisation. This study introduces the Vector Field Heterogeneity (VFH) metric to quantify such disorganisation. The success of the metric is demonstrated through its ability to discriminate between stimulated and non-stimulated epicardial tissue, as well as the characterisation of the progressive disorganisation observed in simulated maps. Furthermore, results indicate the superiority of the VFH metric to the SI index, a widely recognised heterogeneity metric from the literature. Ultimately, the proposed metric emerges as a reliable heterogeneity parameter suitable for its application on small HD grids to locally assess fibrotic or impaired cardiac tissue.

APPENDIX A
STATISTICAL TESTS RESULTS

The decision to use the Wilcoxon Rank-Sum test as a nonparametric alternative to ANOVA lies in the fact that both the VFH and SI values fail to follow a normal distribution. This was proven by the Shapiro-Wilk test and can be visually observed in the QQ plots (Fig. 10(a) and (b)), where the points deviate
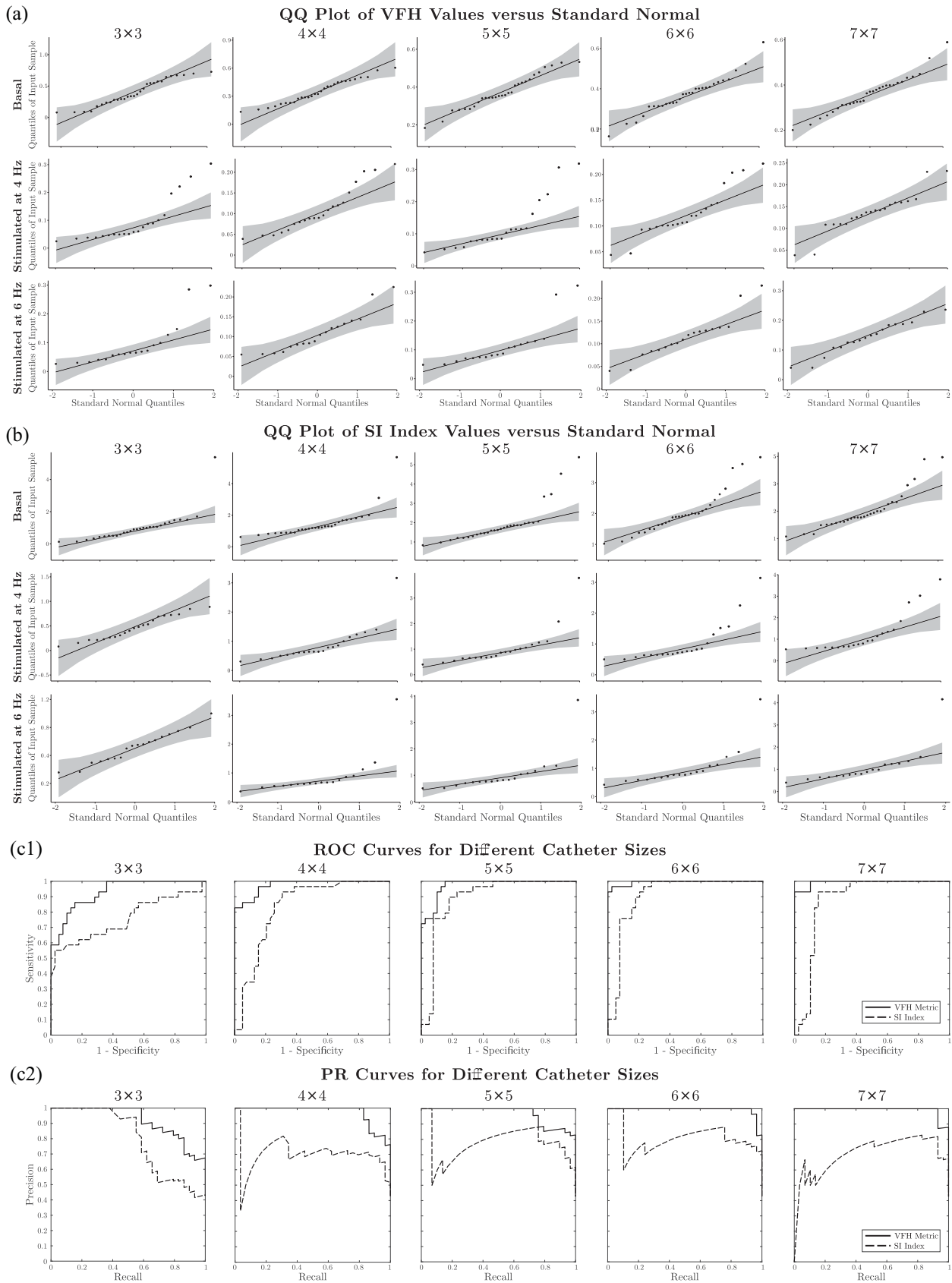
Figure 10. Statistical Test Results; (a) Q-Q Plots of the VFH value samples according to stimulation type (rows) and for different catheter sizes (columns). The 95% confidence interval is indicated by the shaded region; (b) Q-Q Plots of the SI index samples according to stimulation type (rows) and for different catheter sizes (columns). The 95% confidence interval is indicated by the shaded region; (c1) and (c2): Receiver Operating Characteristic (ROC) and Precision-Recall (PR) curves comparison between the VFH metric proposed in this study (solid line) and the SI index (dashed line).

TABLE VIII
P-VALUES OF WILCOXON RANK-SUM TEST FOR COMPARING LAT-DERIVED VFH VALUES ACCORDING TO STIMULATION TYPE

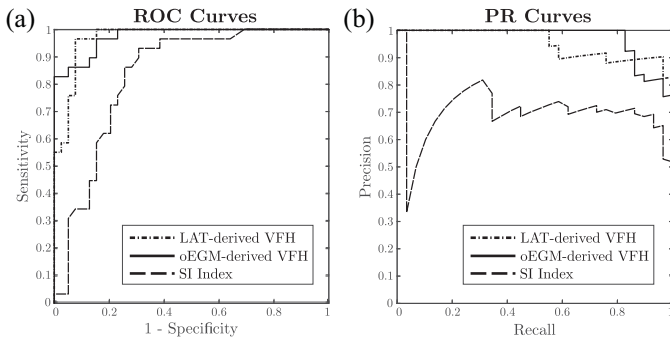| Catheter Size	Basal - Stim. 4 Hz	Basal - Stim. 6 Hz	Stim. 4 Hz - Stim. 6 Hz
3×3	1.1962e-08*	2.8946e-08*	0.3311
4×4	2.3732e-08*	7.7600e-08*	0.7460
5×5	8.4498e-09*	1.9845e-08*	0.5828
6×6	3.7057e-09*	1.3548e-08*	0.3311
7×7	2.5882e-09*	1.1919e-08*	0.5447

∗ p-values < 0.0167

Figure 11. (a) ROC curves comparison between omnipolar-derived and LAT-derived VFH for the case of a 4×4 electrode grid. SI Index results are also displayed; (b) Same comparison for the PR curves.

TABLE IX
P-VALUES OF WILCOXON RANK-SUM TEST FOR COMPARING LAT-DERIVED VFH VALUES ACCORDING TO CATHETER SIZE

Catheter Size	3×3 - 4×4	4×4 - 5×5	5×5 - 6×6	6×6 - 7×7
Basal	0.6632	0.5137	0.9504	0.9380
Stim. 4 Hz	0.3520	0.1824	0.6327	0.3143
Stim. 6 Hz	0.0480	0.0279	0.9370	0.1892

∗ p-values < 0.0125

from the diagonal line. Moreover, the ROC and PR curves corresponding to the values in Table VII are represented in Fig. 10(c).

APPENDIX B
COMPUTATION OF VFH FROM LATs

To eliminate the influence of LAT annotation errors on the superior performance of the proposed metric over the SI, the comparative analysis has been repeated with VFH values resulting from LAT-derived vector maps. The gradient operator is applied to the LAT map and, after normalisation, a vector map representative of the propagation directions is obtained, from which a LAT-derived VFH value is computed. The comparison of these results with the original omnipolar-derived VFH values is displayed in Fig. 9. The performance of the VFH in distinguishing between stimulated and basal maps remains high, as depicted by the low p-values in Table VIII, and the high AUCs in Fig. 11. Additionally, no significant differences are found when comparing results for different catheter sizes (Table IX).

Statement of Contribution

L. Pancorbo and S. Ruipérez-Campillo contributed to the conception and design of the study, mathematics and modelling, data curation and analysis, interpretation of results, code writing and the manuscript writing. A. Tormos, A. Guill, A. Alberola and F. J. Chorro contributed to the performance of the animal experiments. R. Cervigón participated in the conception and design of the study. J. Millet and F. Castells participated in the conception and design of the study, interpretation of results, manuscript writing, supervised and obtained funding for the study. All authors contributed to the article edition and approved the submitted version.

Conflicts of Interest

The authors of this manuscript declare no conflicts of interest.

REFERENCES

[1] R. Jiang, A. D. Beaser, Z. Aziz, G. A. Upadhyay, H. M. Nayak, and R. Tung, "High-density grid catheter for detailed mapping of sinus rhythm and scar-related ventricular tachycardia: Comparison with a linear duodecapolar catheter," *Clin. Electrophysiol.*, vol. 6, no. 3, pp. 311–323, Mar. 2020.

[2] D. C. Deno, R. Balachandran, D. Morgan, F. Ahmad, S. Massé, and K. Nanthakumar, "Orientation-independent catheter-based characterization of myocardial activation," *IEEE Trans. Biomed. Eng.*, vol. 64, no. 5, pp. 1067–1077, May 2017.

[3] S. M. Blanchard, R. J. Damiano, T. Asano, W. M. Smith, R. E. Ideker, and J. E. Lowe, "The effects of distant cardiac electrical events on local activation in unipolar epicardial electrograms," *IEEE Trans. Biomed. Eng.*, vol. BME- 34, no. 7, pp. 539–546, Jul. 1987.

[4] S. Gaeta, T. D. Bahnson, and C. Henriquez, "Mechanism and magnitude of bipolar electrogram directional sensitivity: Characterizing underlying determinants of bipolar amplitude," *Heart Rhythm*, vol. 17, no. 5, pp. 777–785, May 2020.

[5] J. T. Jacobson et al., "Voltage resolution of standard bipolar and omnipolar ventricular electrograms," *Circulation*, vol. 142, no. Suppl_3, Nov. 2020, Art. no. A17013.

[6] S. Haldar et al., "Resolving bipolar electrogram voltages during atrial fibrillation using omnipolar mapping," *Circulation: Arrhythmia Electrophysiol.*, vol. 10, no. 9, Sep. 2017, Art. no. e005018.

[7] A. Porta-Sánchez et al., "Omnipolarity applied to equi-spaced electrode array for ventricular tachycardia substrate mapping," *EP Europace*, vol. 21, no. 5, pp. 813–821, May 2019.

[8] D. Luengo, G. Ríos-Munoz, V. Elvira, C. Sánchez, and A. Artés-Rodríguez, "Hierarchical algorithms for causality retrieval in atrial fibrillation intracavitary electrograms," *IEEE J. Biomed. Health Inform.*, vol. 23, no. 1, pp. 143–155, Jan. 2019.

[9] J. Ng et al., "Measuring the complexity of atrial fibrillation electrograms," *J. Cardiovasc. Electrophysiol.*, vol. 21, no. 6, pp. 649–655, May 2010.

[10] R. Cervigón, J. Moreno, J. García-Quintanilla, J. Pérez-Villacastín, and F. Castells, "Entropy at the right atrium as a predictor of atrial fibrillation recurrence outcome after pulmonary vein ablation," *Biomed. Eng./Biomedizinische Technik*, vol. 61, no. 1, pp. 29–36, Jun. 2016.

[11] E. Cirugeda-Roldán et al., "Characterization of complex fractionated atrial electrograms by sample entropy: An international multi-center study," *Entropy*, vol. 17, no. 11, pp. 7493–7509, Oct. 2015.

[12] A. N. Ganesan et al., "Bipolar electrogram shannon entropy at sites of rotational activation: Implications for ablation of atrial fibrillation," *Circulation: Arrhythmia Electrophysiol.*, vol. 6, no. 1, pp. 48–57, Dec. 2013.

[13] R. Cervigón, J. Moreno, R. B. Reilly, J. Millet, J. Pérez-Villacastín, and F. Castells, "Entropy measurements in paroxysmal and persistent atrial fibrillation," *Physiol. Meas.*, vol. 31, no. 7, Jun. 2010, Art. no. 1011.

[14] K. M. Ropella, A. Sahakian, J. Baerman, and S. Swiryn, "The coherence spectrum. a quantitative discriminator of fibrillatory and nonfibrillatory cardiac rhythms," *Circulation*, vol. 80, no. 1, pp. 112–119, Jul. 1989.

[15] G. W. Botteron and J. M. Smith, "A technique for measurement of the extent of spatial organization of atrial activation during atrial fibrillation in the intact human heart," *IEEE Trans. Biomed. Eng.*, vol. 42, no. 6, pp. 579–586, Jun. 1995.

[16] L. Fendelander, P.-W. Hsia, and R. J. Damiano Jr, "Spatial coherence: A new method of quantifying myocardial electrical organization using multichannel epicardial electrograms," *J. Electrocardiol.*, vol. 30, no. 1, pp. 9–19, Jan. 1997.

[17] G. W. Botteron and J. M. Smith, "Quantitative assessment of the spatial organization of atrial fibrillation in the intact human heart," *Circulation*, vol. 93, no. 3, pp. 513–518, Feb. 1996.

[18] T. H. Everett, L.-C. Kok, R. H. Vaughn, R. Moorman, and D. E. Haines, "Frequency domain algorithm for quantifying atrial fibrillation organization to increase defibrillation efficacy," *IEEE Trans. Biomed. Eng.*, vol. 48, no. 9, pp. 969–978, Sep. 2001.

[19] J. W. Jarman et al., "Organizational index mapping to identify focal sources during persistent atrial fibrillation," *J. Cardiovasc. Electrophysiol.*, vol. 25, no. 4, pp. 355–363, Jan. 2014.

[20] A. G. Kléber, M. J. Janse, F. Wilms-Schopmann, A. Wilde, and R. Coronel, "Changes in conduction velocity during acute ischemia in ventricular myocardium of the isolated porcine heart," *Circulation*, vol. 73, no. 1, pp. 189–198, Jan. 1986.

[21] W. Lammers, M. Schalij, C. Kirchhof, and M. A. Allessie, "Quantification of spatial inhomogeneity in conduction and initiation of reentrant atrial arrhythmias," *Amer. J. Physiol.-Heart Circulatory Physiol.*, vol. 259, no. 4, pp. H1254–H1263, Oct. 1990.

[22] D. Li, S. Fareh, T. K. Leung, and S. Nattel, "Promotion of atrial fibrillation by heart failure in dogs: Atrial remodeling of a different sort," *Circulation*, vol. 100, no. 1, pp. 87–95, Jul. 1999.

[23] S. Verheule et al., "Increased vulnerability to atrial fibrillation in transgenic mice with selective atrial fibrosis caused by overexpression of TGF-β1," *Circulation Res.*, vol. 94, no. 11, pp. 1458–1465, Apr. 2004.

[24] X. Dong, G. Tse, G. Hao, and Y. Du, "Heterogeneities in ventricular conduction following treatment with heptanol: A multi-electrode array study in langendorff-perfused mouse hearts," *Life*, vol. 12, no. 7, May 2022, Art. no. 996.

[25] T. N. Fitzgerald, D. H. Brooks, and J. K. Triedman, "Identification of cardiac rhythm features by mathematical analysis of vector fields," *IEEE Trans. Biomed. Eng.*, vol. 52, no. 1, pp. 19–29, Jan. 2005.

[26] C. Dallet et al., "Cardiac propagation pattern mapping with vector field for helping tachyarrhythmias diagnosis with clinical tridimensional electro-anatomical mapping tools," *IEEE Trans. Biomed. Eng.*, vol. 66, no. 2, pp. 373–382, Feb. 2019.

[27] M. Masè, A. Cristoforetti, M. Del Greco, and F. Ravelli, "A divergence-based approach for the identification of atrial fibrillation focal drivers from multipolar mapping: A computational study," *Front. Physiol.*, vol. 12, Dec. 2021, Art. no. 2347.

[28] A. Guill et al., "QT interval heterogeneities induced through local epicardial warming/cooling. an experimental study," *Revista Española de Cardiología*, vol. 67, no. 12, pp. 993–998, Dec. 2014.

[29] D. C. Deno et al., "High-resolution, live, directional mapping," *Heart Rhythm*, vol. 17, no. 9, pp. 1621–1628, Sep. 2020.

[30] F. Castells et al., "Performance assessment of electrode configurations for the estimation of omnipolar electrograms from high density arrays," *Comput. Biol. Med.*, vol. 154, Mar. 2023, Art. no. 106604.

[31] S. Ruipérez-Campillo et al., "Evaluation and assessment of clique arrangements for the estimation of omnipolar electrograms in high density electrode arrays: An experimental animal model study," *Phys. Eng. Sci. Med.*, vol. 46, pp. 1193–1204, Jun. 2023.

[32] N. M. De Groot et al., "Critical appraisal of technologies to assess electrical activity during atrial fibrillation: A position paper from the European Heart Rhythm Association and European Society of Cardiology Working Group on eCardiology in collaboration with the Heart Rhythm Society, Asia Pacific Heart Rhythm Society, Latin American Heart Rhythm society and computing in cardiology," *EP Europace*, vol. 24, no. 2, pp. 313–330, Dec. 2022.

[33] C. D. Cantwell, C. H. Roney, F. S. Ng, J. H. Siggers, S. J. Sherwin, and N. S. Peters, "Techniques for automated local activation time annotation and conduction velocity estimation in cardiac mapping," *Comput. Biol. Med.*, vol. 65, pp. 229–242, Oct. 2015.

[34] J. P. Ugarte, C. Tobón, and A. Orozco-Duque, "Entropy mapping approach for functional reentry detection in atrial fibrillation: An in-silico study," *Entropy*, vol. 21, no. 2, Jan. 2019, Art. no. 194.

[35] A. S. Jadidi et al., "Functional nature of electrogram fractionation demonstrated by left atrial high-density mapping," *Circulation: Arrhythmia Electrophysiol.*, vol. 5, no. 1, pp. 32–42, Jan. 2012.

[36] U. Richter et al., "A novel approach to propagation pattern analysis in intracardiac atrial fibrillation signals," *Ann. Biomed. Eng.*, vol. 39, pp. 310–323, Aug. 2011.

[37] A. N. Doshi et al., "Feasibility of a semi-automated method for cardiac conduction velocity analysis of high-resolution activation maps," *Comput. Biol. Med.*, vol. 65, pp. 177–183, Oct. 2015.

[38] C. H. Roney et al., "A technique for measuring anisotropy in atrial conduction to estimate conduction velocity and atrial fibre direction," *Comput. Biol. Med.*, vol. 104, pp. 278–290, Jan. 2019.

[39] S. De Jong, T. A. van Veen, H. V. van Rijen, and J. M. de Bakker, "Fibrosis and cardiac arrhythmias," *J. Cardiovasc. Pharmacol.*, vol. 57, no. 6, pp. 630–638, Jun. 2011.

[40] P. Ganesan et al., "Quantifying a spectrum of clinical response in atrial tachyarrhythmias using spatiotemporal synchronization of electrograms," *EP Europace*, vol. 25, no. 5, May 2023, Art. no. euad0558.

[41] Ö. Özgül et al., "High-density and high coverage composite mapping of repetitive atrial activation patterns," *Comput. Biol. Med.*, vol. 159, Jun. 2023, Art. no. 106920.

[42] M. Enokizono and N. Soda, "Direct magnetic loss analysis by FEM considering vector magnetic properties," *IEEE Trans. Magn.*, vol. 34, no. 5, pp. 3008–3011, Sep. 1998.

[43] Y. Tong, S. Lombeyda, A. N. Hirani, and M. Desbrun, "Discrete multiscale vector field decomposition," *ACM Trans. Graph.*, vol. 22, no. 3, pp. 445–452, 2003.

[44] C.-F. Shu and R. C. Jain, "Vector field analysis for oriented patterns," *IEEE Trans. Pattern Anal. Mach. Intell.*, vol. 16, no. 9, pp. 946–950, Sep. 1994.

[45] G. E. Morley, D. Vaidya, F. H. Samie, C. Lo, M. Delmar, and J. Jalife, "Characterization of conduction in the ventricles of normal and heterozygous Cx43 knockout mice using optical mapping," *J. Cardiovasc. Electrophysiol.*, vol. 10, no. 10, pp. 1361–1375, 1999.

[46] S. Massé et al., "Resolving myocardial activation with novel omnipolar electrograms," *Circulation: Arrhythmia Electrophysiol.*, vol. 9, no. 7, 2016, Art. no. e004107.